Interpretation®

Porosity estimation based on rock skeleton general formula and comprehensive pore structure parameter – An application to a tight-sand reservoir

Journal:	*Interpretation*
Manuscript ID	INT-2021-0001.R2
Manuscript Type:	2020-08 Seismic amplitude interpretation for conventional and unconventional resources
Date Submitted by the Author:	01-Sep-2021
Complete List of Authors:	lin, kai; Chengdu University of Technology, College of Geophysics ; The University of Alabama, Department of Geological Sciences He, Xilei; Chengdu University of Technology, College of Geophysics Zhang, Bo; The University of Alabama, Geological Sciences Wen, Xiaotao; Chengdu University Technology, China, He, Zhenhua; Chengdu University of Technology, Liu, Kaiyuan; China National Petroleum Corporation, Geophysical technology research center of BGP INC. Luo, Ceng; PetroChina Southwest Oil & GasField Branch Sichuan Central Oil & Gas Mine Light Hydrocarbon Plant
Keywords:	rock physics, interpretation, 3D, inversion, seismic impedance
Subject Areas:	Application examples (applying a relatively new technique or concept), Case studies

DOI:10.1190/int-2021-0001.1

DOI: 10.1190/INT-2021-0061.1

Porosity estimation based on rock skeleton general formula and comprehensive pore structure parameter – An application to a tight-sand reservoir

Kai Lin[1, 2], Xilei He[1], Bo Zhang[2], Xiaotao Wen[1], Zhenhua He[1], Kaiyuan Liu[3], Ceng Luo[4]

Running Head: Porosity estimation

[1] Chengdu University of Technology, College of Geophysics

[2] University of Alabama, Department of Geological Science

[3]Bureau of Geophysical Prospecting (BGP) Inc.of CNPC, Geophysical technology research center

[4] Petro China Southwest Oil & Gas Field, Central Sichuan Oil and Gas Mine

linkai02102@163.com, hexl@cdut.edu.cn,bzhang33@ua.edu, wenxiaotao@cdut.cn,

hzh@cdut.edu.cn, luochengjhc@petrochina.com.cn

Corresponding author:

Xilei He

Chengdu University of Technology, College of Geophysics

hexl@cdut.edu.cn

DOI: 10.1190/int-2021-0061.1

Porosity estimation based on rock skeleton general formula and comprehensive pore structure parameter – An application to a tight-sand reservoir

Abstract

Most of current 3D reservoir's porosity estimation methods are based on analyzing the elastic parameters inverted from seismic data. It is well-known that elastic parameters vary with pore structure parameters such as pore aspect ratio, consolidate coefficient, critical porosity, etc. Thus, we may obtain inaccurate 3D porosity estimation if the chosen rock physics model fails properly address the effects of pore structure parameters on the elastic parameters. However, most of current rock physics models only consider one pore structure parameter such as pore aspect ratio or consolidation coefficient. To consider the effect of multiple pore structure parameters on the elastic parameters, we propose a comprehensive pore structure (CPS) parameter set that is generalized from the current popular rock physics models. The new CPS set is based on the first order approximation of current rock physics models that consider the effect of pore aspect ratio on elastic parameters. The new CPS set can accurately simulate the behavior of current rock physics models that consider the effect of pore structure parameters on elastic parameters. To demonstrate the effectiveness of proposed parameters in porosity estimation, we use a theoretical model to demonstrate that the proposed CPS parameter set properly addresses the effect of pore aspect ratio on elastic parameters such as velocity and porosity. Then, we obtain a 3D porosity estimation for a tight sand reservoir by applying it seismic data. We also predict the porosity of the tight sand reservoir by using neural network algorithm and a rock physics model that is commonly used in porosity estimation. The comparison demonstrates that predicted porosity has higher correlation with the porosity logs at the blind well locations.

List of Key Words

DOI: 10.1190/INT-2021-0061.1

Extended Gassmann equation, 3D estimation of porosity, pore structure parameters

Introduction

Estimating the reservoir properties from seismic data such as porosity is one of the most important tasks in reservoir characterization. Elastic effective medium theory (EMT) computes the macroscopic properties such as P-impedance and S-impedance that can be inverted from seismic data by incorporation the individual elastic properties of minerals, the volume fractions, and the spatial arrangement of the constituents that make up the rock. The commonly used effective medium theory including Kuster-Toksöz (K-T) model (Kuster and Toksöz, 1974), self-consistent model (Berryman, 1980), and differential effective medium (DEM) model (Berryman, 1992). To simply the commonly used effective medium theory, researchers proposed several approximation approaches (Li and Zhang, 2012; Li et al.,2013; Yang et al., 2014). The approximation is usually based on introducing certain constraints to model that can convert the problem into regular differential question. Researchers also proposed a lot of explicit equations for computing the macroscopic elastic parameters. The commonly models include the Geertsma, Eshelby-Walsh, Hudson, Pride, Nur, Eshelby-Cheng, Sun, Keys-Xu, Hou and multiple porosity variable critical porosity models (Geertsma and Smith 1961; Eshelby, 1957; Walsh, 1965; Hudson, 1992; Pride et al., 2004; Nur et al., 1998; Cheng, 1993; Sun, 2000; Keys and Xu , 2002; Hou et al., 2012; Zhang et al., 2020a, 2020b). The explicitly effective medium equations make it is possible to predict the macroscopic elastic parameters by integrating seismic and petrophysics data.

Biot-Gassmann equation (Biot, 1941) is the most commonly used explicit equation in calculating reservoir properties of dual-phase rocks, such as porosity and bulk modulus of saturated rocks. The dry frame modulus is the most important parameter for Biot-Gassmann

DOI: 10.1190/INT-2021-0061.1

equation. Researchers have developed various kinds of dry frame rock physics models (Eshelby, 1957; Walsh, 1965; Pride et al., 2004; Nur et al., 1998; Sun, 2000; Keys and Xu, 2002; Hou et al., 2012). The pore structure is one of the most important parameters in a dry frame model. The pore structure refers to the pore size, geometry, distribution, and connectivity of between pores, etc. The direct ways to understand the pore structure include optical microscope (OM), scanning electron microscope (SEM), nuclear magnetic resonance (NMR), three-dimensional tomography (3-DCT) and digital imaging analysis (Anselmetti et al., 1998; Weger et al., 2009). Considering that the pore geometry usually is irregular, we often use average pore aspect ratio to represent pore geometry. The consolidation coefficient represents the density and connectivity of pores and cracks and the degree of compaction. The influence of particle contacts and coupling, cementation, and connectivity of the rocks can be represented by the frame flexibility factor. Meanwhile, the critical porosity is used to characterize the initial state of the rocks before compaction and diagenesis.

The research related to the effect of pore structures on the rock elastic properties can be classified into four categories. The first category considers the effect of the pore aspect ratio on rock elastic properties. Cheng and Toksöz (1979) developed a model to invert the pore aspect ratio spectrum, and the inverted results have a very good agreement with SEM measurements. Kumar and Han (2005) established a dual pore aspect ratio model and proposed a porosity inversion method that is based on the DEM model. Li et al. (2021) integrates the differential effective medium model of multiple-porosity rocks, Gassmann equation, Amplitude Versus Offset (AVO) theory, Bayesian theory, and a nonlinear inversion algorithm to simultaneously compute the pore aspect ratio. The second category studies the effect of frame flexibility factor γ_k on rock elastic properties. Based on the theory of pore elasticity, Sun (2000) derived a frame flexibility factor to

DOI: 10.1190/INT-2021-0061.1

describes the effects of particles contacts and particle coupling, cementation, and pore connectivity on the flexibility and elasticity of porous rocks. Dou et al. (2011) first calculated γ_k by analyzing the pore structure of thin sections and then characterized reservoir using the porosity-velocity/permeability crossplot. The third category uses a parameter named critical porosity. Zhang et al. (2012) uses the *P*-wave velocity to invert the critical porosity of the rocks. Li et al. (2019) established the relationship between critical porosity and clay porosity by using a linear fitting. The fourth category considers a parameter named consolidation coefficient. Lee (2006) improved the accuracy of Pride consolidation model by adding a dynamic correction term. Hou et al. (2012) established a comprehensive model by introducing a critical porosity parameter to the Pride model.

Researchers have conducted a lot of research on porosity prediction by using seismic data. AlBinHassan and Wang (2011) using the group method of data handling to predict reservoir porosity. Ba et al. (2013) build multiscale Rock-physics Templates (RPTs), which is based on the Biot-Rayleigh theory, to predict the porosity of carbonate gas reservoirs. Li et al. (2019) use 3D RPTs, which is based on the effective-medium theory and Gassmann equations, to predict porosity of carbonate reservoirs. Wang et al. (2020) use Bayesian discriminant method to predict porosity from the reflectivity method that is estimated elastic parameters. Chen et al. (2020) developed a machine-learning method, which is based on the traditional long short-term memory (LSTM) model, to perform the porosity prediction.

The commonly used parameters that consider the effect of pore structure on the computation of dry frame modulus include pore aspect ratio, consolidation coefficient, critical porosity, the frame flexibility factor. Currently, most of current effective medium theories only consider the effect of one or two pore structure parameters on the macroscopic rock elastic parameters. It is

common that we may need more than one pore structure parameters to consider the effect of pore structure on the macroscopic rock elastic parameters for different scenarios. In this paper, we conducted a thorough review for the current methods of dry frame modulus computation. Then, we proposed a comprehensive pore structure (CPS) parameter that can consider pore structure parameters such as pore aspect ratio, consolidation coefficient, critical porosity, and the frame flexibility factor after one-step simplification. Finally, we applied our theory to predict the porosity of a tight-sand reservoir.

Effect of Pore System on the Rock Elastic Properties

Gassmann equation is the most used explicit equation that describes the relationship among effective bulk modulus of a saturated rock K_{sat}, bulk modulus of solid matrix K_0, bulk modulus of dry frame K_{dry}, bulk modulus of fluid K_{fl}, and porosity ϕ (Berryman, 2009)

$$\frac{K_{sat}}{K_0 - K_{sat}} = \frac{K_{dry}}{K_0 - K_{dry}} + \frac{K_{fl}}{\phi(K_0 - K_{fl})}. \quad (1)$$

By re-arranging Equation 1, we can compute the porosity of a rock if we know bulk modulus of the solid matrix, saturated rock, dry frame, and saturated fluids,

$$\phi = \frac{K_{fl}(K_0 - K_{sat})(K_0 - K_{dry})}{K_0(K_0 - K_{fl})(K_{sat} - K_{dry})}. \quad (2)$$

The bulk modulus parameters of saturated rock can be calculated using the *P*- and *S*-wave velocity and density that are inverted from seismic data or well logging data. The modulus of dry frame is a function of porosity, pore geometry, mineral composition, and other parameters. It is well-known that it is challenging to obtain an accurate estimation of dry frame modulus. The most used rock physics models that characterize the relationship between pore structure and dry frame modulus are listed as follows (Eshelby, 1957; Walsh, 1965; Pride et al., 2004; Nur et al., 1998; Sun, 2000; Keys and Xu, 2002; Hou et al., 2012):

DOI: 10.1190/INT-2021-0061.1

Eshelby-Walsh model: $$K_{dry} = K_0 \frac{1}{1 + \frac{m}{\alpha}\phi}, \quad (3)$$

Pride model: $$K_{dry} = K_0 \frac{1-\phi}{1 + c\phi}, \quad (4)$$

Nur model: $$K_{dry} = K_0(1 - \phi/\phi_c), \quad (5)$$

Hou model: $$K_{dry} = K_0 \frac{1 - \phi/\phi_c}{1 + c\phi/\phi_c}, \quad (6)$$

Keys-Xu model: $$K_{dry} = K_0(1-\phi)^w, \quad (7)$$

Sun model: $$K_{dry} = K_0(1-\phi)^{\gamma_k}, \quad (8)$$

where m is a function of the Poisson's ratio of solid matrix and α is pore aspect ratio, c is the consolidation coefficient, ϕ_c is the critical porosity, w is a function of the pore aspect ratio and Poisson's ratio (Chen and Huang,2001), and $\gamma_k$is the frame flexibility factor (Sun, 2000). He et al. (2012) establishes a rock skeleton general formula based on the studies of the above equations,

$$K_{dry} = K_0 \frac{1 - p\phi}{1 + q\phi}, \quad (9)$$

where p and q are dimensionless parameters. Note that Equation 9 can be simplified to Equations 3-6 by setting q and p to a proper value set (Table 1). The value of w of Equation 7 and γ_k of Equation 8 both ranges from 2 to 10 (Sun,2000). Thus, the exponential term in Equations 7 and 8 will be a small value and we can approximate the exponential term by adopting the first few terms after Taylor expansion.

Let's set $f(\phi) = (1-\phi)^w$ and take a Taylor series expansion of $f(\phi)$ at $\phi = \phi_z$, then:

$$f(\phi) = (1-\phi_z)^w - w(1-\phi_z)^{w-1}(\phi - \phi_z) + \cdots + (-1)^2 \frac{\prod_{i=1}^{n}(w-i+1)}{n!}(1-\phi_z)^{w-n}(\phi-\phi_z)^n + R_n(\phi), \quad (10)$$

DOI: 10.1190/INT-2021-0061.1

where $R_n(\phi)$ is the residual term. Considering that tight reservoir usually has very small porosity, we propose to expand the equation at $\phi_z = 0$ and ignore higher order terms

$$f(\phi) = 1 - w\phi\,. \tag{11}$$

Then, Equation 7 can be simplified as follow

$$K_{dry} = K_0(1 - w\phi). \tag{12}$$

Note that Equation 9 can be used to approximate Keys-Xu's mode when $q = 0$ and $p = w$. Similarly, Equation 9 can also be used to approximate Sun's model when $q = 0$ and $p = \gamma_k$.

To evaluate accuracy of Equation 11, we compare the effective *P*-wave velocities before (Equation 7) and after (Equation 12) approximation for a typical model in Table 2, (Mavko et al.,2003). Figure 1a shows the relative error of effective *P*-wave velocity using Equation 11. The vertical axis of Figure 1a are the relative error in percentage. The relative error is defined as ratio between the effective velocity computed using Equation 12 and effective velocity computed using Equation 7. The horizontal axes of Figure 1a are porosity and pore aspect ratio. Note that the porosity value range is set between 0.01 and 0.08 considering that our research target is tight sand reservoir. Figure 1a demonstrate that the maximum relative velocity error is 0.7%. The vertical bars in Figure 1b show the frequency distribution histogram of the relative velocity error. The blue line in Figure 1b shows the accumulated frequency. Note that more than 92% of the velocity error is less than 0.25%. The 0.25% relative error corresponds to 12.5 m/s if the velocity of the sandstone reservoir is 5000 m/s. Figure 1 indicates that Equation 12 can well approximate the relationship between pore aspect ratio and rock elastic properties. Therefore, we conclude that Equation 9 can be used to represent the equations 3-8 if we set the two parameters to a proper value set. In this paper, we use Equation 9 to estimate the bulk modulus of the rock's dry frame.

By re-arranging equation 1, we obtain:

DOI: 10.1190/int-2021-0061.1

$$K_0(K_{sat}-K_{dry})\phi(K_0-K_{fl}) = (K_0-K_{sat})(K_0-K_{dry})K_{fl}. \quad (13)$$

By substituting the dry frame, Equation 13 becomes as follow,

$$K_0(K_{sat}-K_0\frac{1-p\phi}{1+q\phi})\phi(K_0-K_{fl}) = (K_0-K_{sat})(K_0-K_0\frac{1-p\phi}{1+q\phi})K_{fl}. \quad (14)$$

Finally, we obtain the porosity as a function of rock parameters as follow

$$\phi = \frac{(K_0-K_{sat})[(p+q)K_{fl}+(K_0-K_{fl})]}{(K_0-K_{fl})(qK_{sat}+pK_0)}. \quad (15)$$

We denote $S = p + q$, which is a comprehensive pore structure (CPS) parameter in this paper. The Equation is further re-arranged as follows

$$\phi = \frac{(K_0-K_{sat})[SK_{fl}+(K_0-K_{fl})]}{(K_0-K_{fl})SK_0[1-\frac{q(K_0-K_{sat})}{(p+q)K_0}]}. \quad (16)$$

Since the value of $q/(p+q)$ are either 0 or 1(See from table1), the equation 16 can be expressed as

$$\phi = \begin{cases} \frac{(K_0-K_{sat})[SK_{fl}+(K_0-K_{fl})]}{(K_0-K_{fl})SK_0} & if \quad q/(p+q)=0 \\ \frac{(K_0-K_{sat})[SK_{fl}+(K_0-K_{fl})]}{(K_0-K_{fl})SK_0} & if \quad q/(p+q)=1 \end{cases}. \quad (17)$$

Note that Equation 17 can successfully substitute Nur's, Keys-Xu's, and Sun's models when $q/(p+q)=0$. Equation 17 also can represent Pride's, Eshelby-Walsh's, and Hou's model when $q/(p+q)=1$. Equation (16) and (17) becomes unified equation by adding an adjustment parameter Ap,

$$\phi = \frac{(K_0-K_{sat})[SK_{fl}+(K_0-K_{fl})]}{(K_0-K_{fl})S[ApK_{sat}+(1-Ap)K_0]}. \quad (18)$$

Finally, we obtain the defined CPS parameter as follow

$$S = \frac{(K_0-K_{fl})(K_0-K_{sat})}{\phi[ApK_{sat}+(1-Ap)K_0](K_0-K_{fl})-K_{fl}(K_0-K_{sat})}, \quad (19).$$

DOI: 10.1190/int-2021-0061.1

Equation 19 demonstrate that the CPS can be used to describe critical porosity ϕ_c,frame flexibility factor γ_k, and pore aspect ratio α, if we set $Ap = 0$. The defined CPS parameter can also be used to describe consolidation coefficient c, $\frac{m}{\alpha}$, and Hou's model when we set $Ap = 1$. In this paper, the value of adjustment parameters Ap range from 0 to 1. Equation 18 demonstrates that it contains information about the pore structure and can be used to predict porosity from seismic data.

To demonstrate that we can use Equation 18 in predicting reservoir porosity, we apply it to a set of models whose dry frame parameters are shown in Table 2. The porosity of the models varies from 0.01 to 0.1, and the pore aspect ratio of the models varies from 0.02 to 0.08. The dry frame bulk modulus and saturated rock modulus in Equation 1 are computed using Equations 7 and 1, respectively. The adjustment parameters Ap in equation 18 is set as 0.5. The relative porosity error is defined as ratio between predicted porosity error and true porosity. Figure 2a demonstrate that the maximum relative error of predicted porosity is 5% with an average value of 2.67%. Figure 2b shows the porosity error histogram and the blue line represent the accumulated frequency. Note that more than 70% of the predicted porosity has a relative error smaller than 3%. The low errors in Figure 2 demonstrates that the proposed equation provides a good approximate on porosity. Thus, we can use Equation 18 to predict the porosity of reservoir if we can obtain a good estimation for the dry frame modulus, saturated rock modulus, and fluid modulus.

Field Data Example

The research area is located within the middle of Sichuan Basin (Figure 3a). The size of the seismic survey is about 61.5 K_m^2. There are three exploration wells named as JY1, JY2 and JY3 (Figure 3b) within the seismic survey. The interval of interest is the second group of the upper

DOI: 10.1190/INT-2021-0061.1

Triassic Xujiahe formation (labeled as X2). The depositional environment is braided river delta-lake with a typical sand-mudstone inter bedded formations. Based on the cores and scanning electron microscopes, the pore type of X2 can be divided into primary pore, secondary pore, and fractures. The pores are mainly inter-particle pores (filled with heterobase, cement, and siliceous materials). The rest of pores are residual inter-particle and intra-particle dissolved pores (figure 4). The core analysis indicates that majority of fractures are horizontals and low oblique fractures, horizontal interlayer fractures and structural fractures (Figure 5). The X2 formation reservoir has low porosity and low permeability. The porosity estimated from core ranges from0.02 to 0.17, with an average of 6.38%. The core permeability ranges from 0.1 to 1.0^3 mD, with an average of 0.33 millidarcy (mD) (Figure 6).

Figures 7a and 7b show statistical frequency distribution of porosity and *P*-wave velocities of three wells. The reservoir porosity varies from 0.025 to 0.14, with an average of 0.07. The non-reservoir has porosity ranging between 0.01 and 0.08, with an average of 0.045. The average relative porosity difference of is 35%, which is much higher than the 3% relative error caused by the proposed general method. On the other hand, the reservoir velocity ranges from 4500 to 5000 m/s, with an average of 4713 m/s. The non-reservoir velocity varies from 4600 to 5000 m/s, with an average of 4880 m/s. The velocity difference is 167 m/s, which is much higher than the error of 12.5 m/s introduced by the proposed general formula. Therefore, the proposed method can be used to predict the porosity of tight sand reservoir.

According to wells analysis, we set the CPS value as 3.0 in our porosity inversion process. Figure 10 shows the predicted porosity using two different methods. The red curve in Figure 10 is the predicted porosity by linear fitting the *P*-wave velocity and porosity well logs. The blue cure in Figure 10 is the predicted porosity by applying our method to the *P*-wave, *S*-wave, and density

DOI: 10.1190/INT-2021-0061.1

logs. The predicted porosity of linear fitting method is consistent with the original porosity but has large errors for several zones indicated by purple rectangles. The predicted porosity using our method has a better correlation with the well log porosity. The black arrows in Figure 10 indicate the minor error predicted by our method. Note that our predicted result has errors at zones that have relatively low or high porosity values. Figure 8 indicates that the CPS values of zones, which have relatively low or high porosity values, are close to 2.0 and 6.0. However, we use a 3.0 value of CPS parameter in the inversion.

To obtain a 3D porosity estimation, we first compute the *P*-wave, *S*-wave, and density using prestack simultaneous inversion. We only used YJ1 and YJ3 wells in the process of prestack inversion and YJ2 well is used as a blind well. Figure 11 shows the prestack inversion analysis for YJ1 and JY3 wells. Note that there is a good match between the inverted P-impedance (red curve) and P-impedance log (blue curve). The black curves in Figure 11 are the low frequency model used for the prestack inversion. Figures 12a, 12b, and 12c show the inverted P-impedance, S-impedance, and Density of cross-well section, respectively.

Finally, we predict the porosity by applying the proposed method to the inverted elastic parameters. The fluid modulus K_{fl} is set as 0.336 Gpa. The solid matrix modulus K_0 take the average value of the inversion solid matrix modulus (Lin et al., 2011) of the target interval and is set as 37.9 Gpa. Figure 13 shows a section of inverted porosity that across the three wells. For comparison, the post stack probabilistic neural networks (PNN), multi-layer feed forward neural networks (MLFN) and Eshelby-Walsh(E-W) model are used to predict the porosity. The red and blue rectangles in Figure 13 indicate the high and low gas production zones, respectively. Note that there is a good match between high porosity zones predicted using our method and high gas production zones. However, the predicted results from other three method have lower correlation

DOI: 10.1190/INT-2021-0061.1

between the high porosity zones and high gas production zones. Figure 14 shows the predicted porosity (blue curves) at wellbore locations and well log porosity (red curves). Note that the predicted result from two neural network methods have relatively poor correlation with the porosity logs. The predicted result from Eshelby-Walsh(E-W) model has acceptable correlation and the predicted result from our method has the best correlation among all methods.

Figure 15 shows the strata slices of predicted porosity within in the X2 formation. The porosity of the upper part of X2 formation is higher than that of the lower part. The gas production of Well JY1 and JY2 are $52*10^4$ m^3 and $20*10^4$ m^3 per day, respectively. Unfortunately, Well JY3 is a dry well. Figure 15 indicates that wells JY1, YJ2, and YJ3 are located at the high porosity, medium porosity, and low porosity zones, respectively.

Discussion

In this paper, we proposed a new CPS parameter to consider the effect of pore structure on the effective parameters of rocks. However, our method uses constant CPS and the dry frame modulus K_0 in the real application. Thus, we can obtain an inaccurate estimation if the pore structures or mineral components have obvious changes with locations. Thus, the constant parameters may vary with depositional environments or facies. Our method also has requirement about petrophysics data. Our method needs P-wave, S-wave, density, and water saturation logs to determine the dry frame modulus. The fluids modulus K_{fl} is usually measured in the Laboratory. In this paper, we take the value of 0.336 Gpa for modulus K_{fl}. Again, the fluids modulus may vary with cases.

Note the defined CPS parameter is a function of dry frame modulus, saturated modulus, fluid modulus, and porosity. Thus, CPS parameter vary with matrix and fluid modulus. Figures 17 and 18 shows the effect of matrix and fluid modulus on the CPS parameter for well JY1, respectively.

DOI: 10.1190/INT-2021-0061.1

In this study, the CPS parameter, matrix modulus and fluid modulus are 3, 37.9 GPa and 0.0336 GPa, respectively. To exam the effect of CPS on the accuracy of porosity prediction, we set constant value to matrix/fluid modulus and perturbation the CPS with (a) -20 % (the first panel in Figure 16), (b) -10 % (the second panel in Figure 16), (c) 10 % (the third panel in Figure 16), (d) 20 % (the fourth panel in Figure 16), Figure 16 demonstrates that our method fails to produce accurate prediction if the error of CPS reaches 20% (Figure 16a and 16d). Thus, we conclude that our predicted porosity should have obvious errors if the corresponding CPS value of reservoir is great than 3.6 or smaller than 2.4. Figure 17 shows the effect of fluid modulus on the accuracy of porosity prediction. The matrix modulus and CPS are set to be constant values in Figure 17, and we perturbation the fluid modulus with (a) -20 % (the first panel in Figure 17), (b) -10 % (the second panel in Figure 17), (c) 10 % (the third panel in Figure 17), (d) 20 % (the fourth panel in Figure 17). Note that the predicted porosity error is very small even we have errors in the estimation of fluid modulus. Figure 17 indicates that our method is less sensitive to the fluid modulus. Figure 18 shows the effect of matrix modulus on the accuracy of predicted porosity. The fluid modulus and CPS parameter are set to be constant, and the matrix modulus is perturbated by (a) -5 % (the first panel in Figure 18), (b) -2 % (the second panel in Figure 18), (c) 2 % (the third panel in Figure 18), (d) 5 % (the fourth panel in Figure 18). Note that even a small error (±2%) in the matrix modulus would cause obvious error in the porosity estimation. Figure 18 shows that our method is very sensitive to the error of matrix modulus.

Conclusions

We introduce a comprehensive pore structure parameter, CPS, to consider the effect of pore structure on the effective parameter of rocks. The application demonstrates that our proposed method can be used to predict the porosity if we set a proper value to CPS parameter. The predicted

result demonstrates that the CPS parameter can improve the accuracy of porosity prediction. However, our method is sensitive to the matrix modulus. The sensitivity analysis indicate that the method needs an accurate estimation of elastic parameters in predicting the reservoir porosity. The most common parameters affect the matrix modulus include mineral components and porosity. Thus, we may need to use a variable matrix modulus if the study targets have obvious depositional environmental changes.

Data and Materials Availability

Data associated with this research are confidential and we cannot release them for public.

DOI: 10.1190/INT-2021-0061.1

DOI: 10.1190/INT-2021-0061.1

References

AlBinHassan, N., and Y. Wang, 2011, Porosity prediction using the group method of data handling: Geophysics, **76**, no. 5, O15-O22.

Anselmetti, F., S. Luthi, and G. Eberli,1998, Quantitative Characterization of Carbonate Pore Systems by Digital Image Analysis: AAPG Bulletin, **82**, no. 10, 1815-1836.

Ba, J., H. Cao, J. M. Carcione, G. Tang, X. Yan, W. Sun, and J. Nie, 2013, Multiscale rock-physics templates for gas detection in carbonate reservoirs: Journal of Applied Geophysics, **93**, 77-82.

Berryman, J., 1980, Long-wavelength propagation in composite elastic media II. Ellipsoidal inclusions: The Journal of the Acoustical Society of America, **68**, no. 6, 1820-1831.

Berryman, J., 1992, Single-scattering approximations for coefficients in Biot's equations of poroelasticity: The Journal of the Acoustical Society of America, **91**, no. 2, 551-571.

Biot, M., 1941, General theory of three dimensional consolidation: Journal of Applied Physics, **12**, no. 2, 155-164.

Chen, R., and T. Huang, 2001, Petrophysics: Peking University Press, Beijing.

Cheng, C., and M. N. Toksöz, 1979, Inversion of seismic velocities for the pore aspect ratio spectrum of a rock: Journal of Geophysical Research, **84**, no. 13, 675-684.

Cheng, C., 1993, Crack models for a transversely isotropic medium: Journal of Geophysical Research, **98**, No. B1, 675-684.

Chen. W., L. Yang, B. Zha, M. Zhang, and Y. Chen, 2020, Deep learning reservoir porosity prediction based on multilayer long short-term memory network: Geophysics, **85**, no. 4, WA213-WA225.

Dou, Q., Y. Sun, and C. Sullivan, 2011, Rock-physics based carbonate pore type characterization and reservoir permeability evaluation, upper San Andres reservoir, Permian Basin, west Texas: Journal of Applied Geophysics, **74**, no. 1, 8-18.

Eshelby, J., 1957, The determination of the elastic field of an ellipsoidal inclusion and related problems: Proceedings of the Royal Society, Series A, Mathematical, Physical and Engineering Sciences, **241,** no. 1226, 376-396.

Geertsma, J., and D. Smith, 1961, Some aspects of elastic wave propagation in fluid saturated porous solids: Geophysics, **26**, no. 2, 169-182.

He, X., Z. He, X. Wang. X. Xiong, and L. Jiang, 2012, Rock skeleton models and seismic porosity inversion: Applied Geophysics, **9**, no. 3, 349-358.

Hou, B., X. Chen, and X. Zhang, 2012, Critical porosity Pride model and its application: Oil Geophysical Prospecting, **47**, no. 2, 277-281.

Hudson, J., 1992, Overall elastic properties of isotropic materials with arbitrary distribution of circular cracks: Geophysical Journal International, **102**, no. 2, 465-469.

James G. B., 1999, Origin of Gassmann's equations: Geophysics, **64**: 1627-1629.

Keys, R., and S. Xu, 2002, An approximation for the Xu-White velocity model: Geophysics, **67**, no. 5, 1406-1414.

Kumar, M., and D. Han, 2005, Pore shape effect on elastic properties of carbonate rocks: SEG Technical Program Expanded Abstracts, 1477-1481, Houston.

DOI: 10.1190/INT-2021-0061.1

Küster, G., and M. N. Toksöz, 1974, Velocity and attenuation of seismic waves in two phase media: Part1. Theoretical formulation: Geophysics, **39**, no.5, 587-606.

Lee, M., 2006, A simple method of predicting S-wave velocity: Geophysics, **71**, no. 6, 161-164.

Li, H., and J. Zhang, 2012, Analytical approximations of bulk and shear moduli for dry rock based on the differential effective medium theory: Geophysical Prospecting, **60**, no. 2, 281-292.

Li, H., J. Zhang, and F. Yao,2013, Inversion of effective pore aspect ratios for porous rocks and its applications: Chinese Journal of Geophysics, 56, no. 2, 608-615.

Li, H., J. Zhang, S. Cai, and H. Pan, 2019, 3D rock physics template for reservoirs with complex pore structure: Chinese Journal of Geophysics, **62**, no. 7, 2711–2723.

Li, H., J. Zhang, H. PAN, and Q. Gao,2021, Nonlinear simultaneous inversion of pore structure and physical parameters based on elastic impedance: Science China Earth Sciences, **64**, No. 6, 977-991.

Li, N., H. Chen, X. Zhang, J. Han, J. Wang, and X. Wang,2019, Simultaneous prediction of rock matrix modulus and critical porosity: Applied Geophysics, 2019, **16**, no. 1, 15-26.

Lin, K., X. Xiong, X. Yang, Z. He, and J. Cao, 2011, Self-adapting extraction of matrix mineral bulk modulus and verification of fluid substitution: Applied Geophysics, **8**, no. 2, 110-116.

Mavko, G., T. Mukerji, and J. Dvorkin, 1998, The Rock physics handbook: Tools for seismic analysis in porous media: Cambridge University Press.

Nur, A., G. Mavko, J. Dvorkin, and D. Gal, 1998, Critical porosity: The key to relating physical properties to porosity in rocks: The Leading Edge, **17**, no. 3, 357-362.

Pride, S., J. Berryman, and J. M. Harris, 2004, Seismic attenuation due to wave-induced flow: Journal of Geophysical research, 109, B01201.

Sun, Y., 2000, Core-log-seismic integration in hemipelagic marine sediments on the eastern flank of the Juan de Fuca Ridge, in Fisher, A., Davis, E. E., and Escutia, C, Eds., Proceedings of Ocean Drilling Program, Scientific Results, 168: Texas A&M, College Station TX, 21–35.

Walsh, J., 1965, The effective of cracks on the compressibility of rock: Journal of Geophysical Research, **20**, no. 2, 381-384.

Wang, P., X. Chen, J. Li, and B. Wang, 2020, Accurate porosity prediction for tight sandstone reservoir: A case study from North China: Geophysics, **85**, no. 2, B35-B47.

Weger, R., G. P. Eberli, G. T. Baechle, J. Massaferro, and Y. Sun, 2009, Quantification of pore structure and its effect on sonic velocity and permeability in carbonates: AAPG Bulletin, **93**, no. 10, 1297-1317.

Yang, F., X. Yin, and B. Liu, 2014, The research of variable dry rock matrix equivalent model: Geophysical prospecting for petroleum, **53**, no. 3, 280-286.

Zhang, J., H. Li, and F. Yao, 2012, Rock critical porosity inversion and S-wave velocity prediction: Applied Geophysics, **9**, no. 1, 57-64.

Zhang, J., X. Yin, and G. Zhang, 2020, Rock physics modelling of porous rocks with multiple pore types: a multiple-porosity variable critical porosity model: Geophysical Prospecting, **68**, 955-967.

Zhang, J., X. Yin, G. Zhang, Y. Gu, and X. Fan,2020. Prediction method of physical parameters based on linearized rock physics inversion: Petroleum Exploration and Development, **47**, no. 1, 59-67.

DOI: 10.1190/INT-2021-0061.1

List of Figures

Figure 1. Relative *P*-wave velocity error varying with porosity and pore aspect ratio. (a) The relative *P*-wave velocity, varying with porosity and pore aspect ratio. The relative *P*-wave velocity is computed using Equation 12. (b) The histogram of relative *P*-wave velocity.

Figure 2. (a) The relative error of porosity predicted by using proposed method. (b) The frequency histogram of relative porosity error.

Figure 3. (a) The regional map of Sichuan Basin. (b) The structural map of the top of the Xujiahe formation, the color bar represents the two-way travel time of the structural map time.

Figure 4. The statistics of reservoir porosity type based the cores of the X2 formation. The main pore type is inter-particle pores filled with heterobase.

Figure 5. (a) Representative cores and (b) thin sections of the X2 formation. (a) The cores with horizontal and low dipping angle fractures (indicated by the red arrows). (b) The thin section demonstrating the dissolved pores that were filled by the blue feldspars (indicated by the green arrows) and micro fractures.

Figure 6. Histogram of (a) the core porosity and (b) core permeability of the X2 formation.

Figure 7. The histogram of porosity and *P*-wave logs for the X2 formation. (a)Histogram of porosity log. (b)Histogram of logging *P*-wave. The blue and red bars are the histogram for the well logs of non-reservoir and reservoir, respectively.

Figure 8. The well logs of (a) YJ3, (b) YJ2, and (c) YJ2. The red and blue curves in the first panel are *P*-wave and *S*-wave velocities, respectively. The red and blue curves in the second panel are density and Gamma-Ray logs. The third, fourth, and fifth panel are porosity, CPS, and pore aspect ratio, respectively. The red and blue blocks in the sixth panel represent high and low production zones.

DOI: 10.1190/INT-2021-0061.1

Figure 9. The CPS parameter varying with pore aspect ratio for different lithologies. The red, blue, and black dash lines show the CPS parameter varies with pore aspect ratio for dolomites, sandstone, and limestone, respectively

Figure 10. The comparison of predicted porosity at well (a) YJ3, (b) well YJ1, and (c) YJ2, respectively. The red, blue, and green curves are the porosity log, predicted porosity using our method, and inverted porosity using learning fitting. The black arrows indicate the negligible errors produced by our method. The purple rectangles indicate the obvious inaccurate prediction using linear fitting.

Figure 11. Prestack AVO inversion analysis at (a)YJ1 and (b)YJ3 well. The red, blue, and black curves are the inverted, original well log, and low-frequency component of well log, respectively. The red and black seismic traces are the synthetic and real seismic data.

Figure 12. The inverted sections of (a) P-impedance, (b)S-impedance and (c)Density. The gas (red square) and low gas producing layers (blue square) correspond to the low impedance and density area.

Figure 13. The vertical section of predicted porosity using (a) proposed method, (b) probabilistic neural network, (c) multi-layer feed forward network, and (d) the Eshelby-Walsh model, respectively. The horizontal blue curves are the strata horizons. The red and blue arrows indicate high and low production zones.

Figure 14. The comparison of predicted porosities (red curves) and porosity log (blue curves) at (a) well YJ3, (b) well YJ1, and (c) YJ2. The blue curves in the first, second, third, fourth panels are predicted porosity using proposed method, PNN, MLFN, and E-W model, respectively. The red, blue and green arrows indicate the zones that has relatively high predicted error.

Figure 15. The strata slices of predicted porosity within the target zones.

DOI: 10.1190/INT-2021-0061.1

Figure 16. The sensitive analysis for the effect of CPS parameter on porosity prediction. We perturbation the CPS with (a)-20 %, (b) -10 %, (c) 10 %, and (d) 20 %. The red curves are the porosity log and blue curves are predicted porosity using our method, respectively.

Figure 17. The sensitive analysis for the effect of fluid modulus on porosity prediction. We perturbation the fluid modulus with (a)-20 %, (b) -10 %, (c) 10 %, and (d) 20 %. The red curves are the porosity log and blue curves are predicted porosity using our method, respectively.

Figure 18. The sensitive analysis for the effect of matrix modulus on porosity prediction. We perturbation the matrix modulus with (a)-20 %, (b) -10 %, (c) 10 %, and (d) 20 %. The red curves are the porosity log and blue curves are predicted porosity using our method, respectively.

DOI: 10.1190/int-2021-0061.1

List of Figures

Table 1. The Relationship between the skeleton general formula and different dry frame modulus models.

Table 2. Parameters of the pure quartz model, gas-bearing reservoir, $K_{fl}$is the bulk modulus of gas.

DOI: 10.1190/INT-2021-0061.1

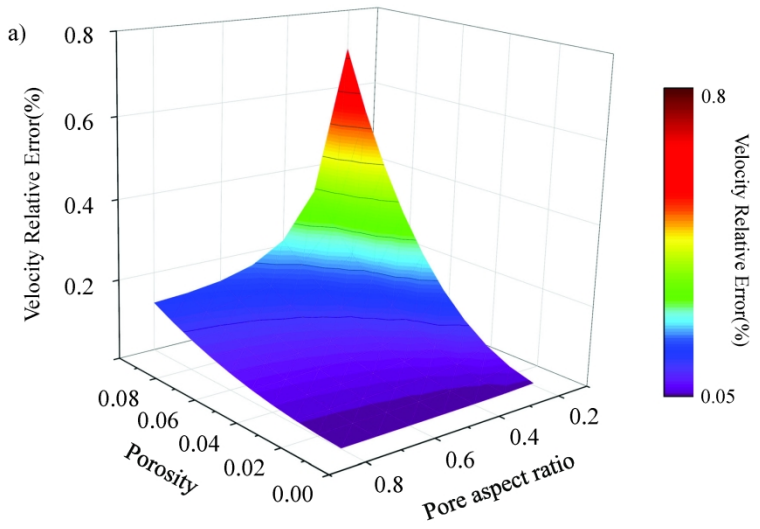

Figure 1a

Figure 1a. Relative P-wave velocity error varying with porosity and pore aspect ratio. (a) The relative P-wave velocity, varying with porosity and pore aspect ratio. The relative P-wave velocity is computed using Equation 12. (b) The histogram of relative P-wave velocity.

279x215mm (300 x 300 DPI)

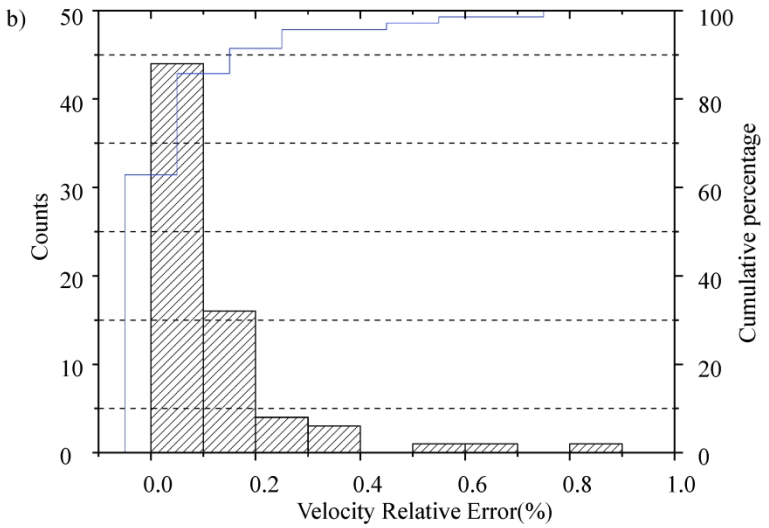

Figure 1b

Figure 1b. Relative P-wave velocity error varying with porosity and pore aspect ratio. (a) The relative P-wave velocity, varying with porosity and pore aspect ratio. The relative P-wave velocity is computed using Equation 12. (b) The histogram of relative P-wave velocity.

279x215mm (300 x 300 DPI)

DOI: 10.1190/INT-2021-0061.1

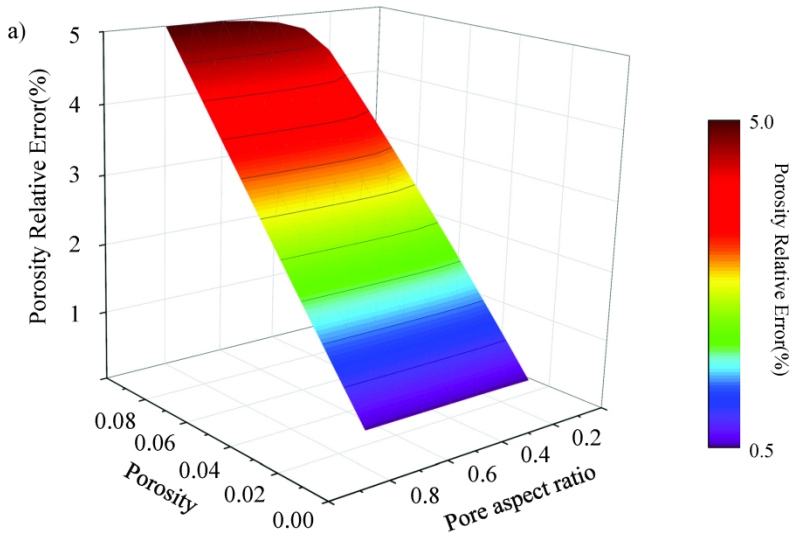

Figure 2a

Figure 2a. (a) The relative error of porosity predicted by using proposed method. (b) The frequency histogram of relative porosity error.

279x215mm (300 x 300 DPI)

DOI: 10.1190/INT-2021-0061.1

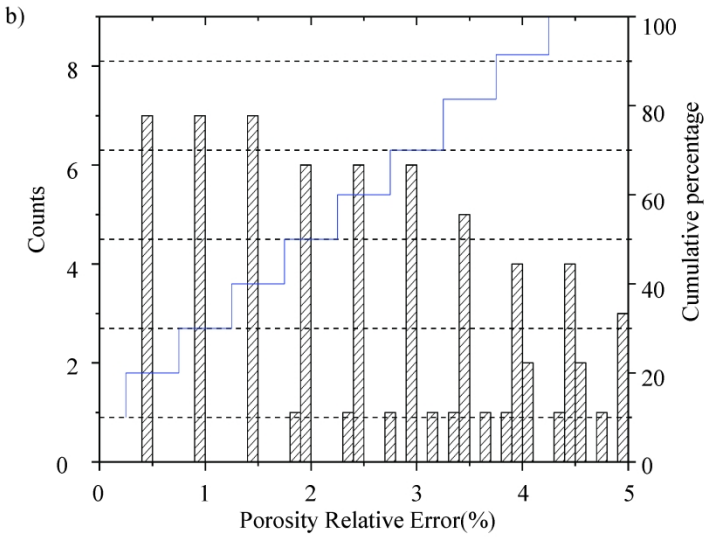

Figure 2b

Figure 2b. (a) The relative error of porosity predicted by using proposed method. (b) The frequency histogram of relative porosity error.

279x215mm (300 x 300 DPI)

DOI: 10.1190/INT-2021-0061.1

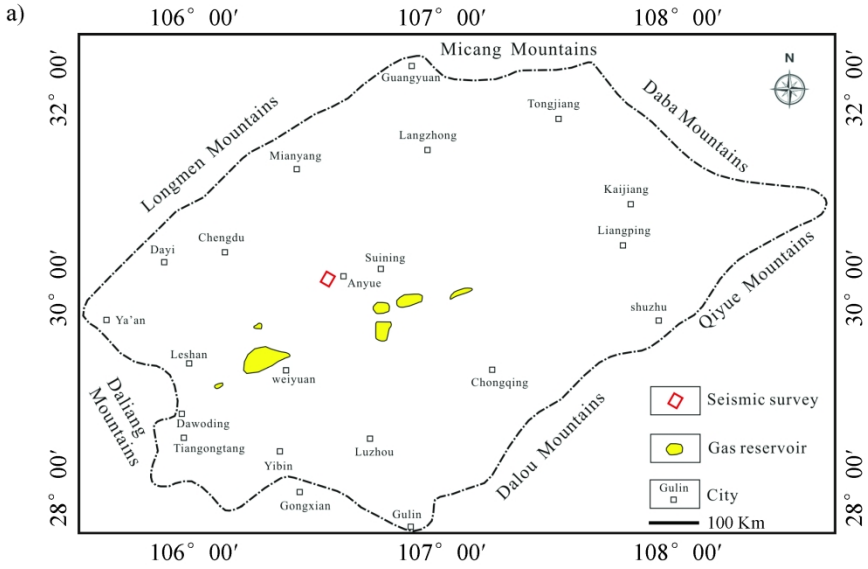

Figure 3a

Figure 3a. (a) The regional map of Sichuan Basin. (b) The structural map of the top of the Xujiahe formation, the color bar represents the two-way travel time of the structural map time.

279x215mm (300 x 300 DPI)

DOI: 10.1190/INT-2021-0061.1

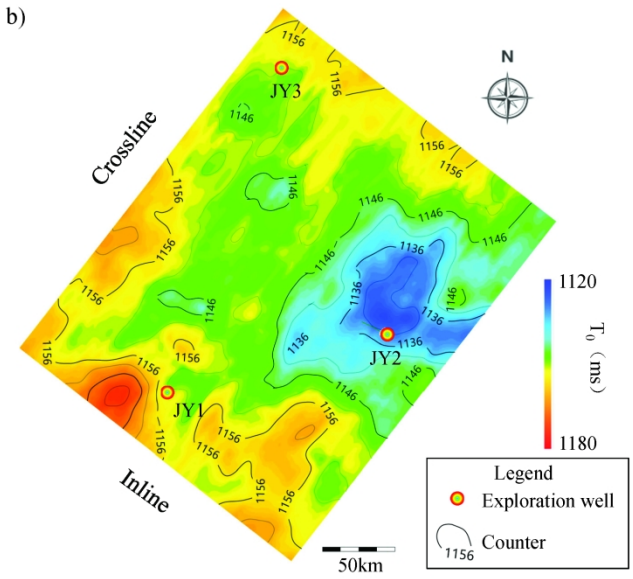

Figure 3b

Figure 3b. (a) The regional map of Sichuan Basin. (b) The structural map of the top of the Xujiahe formation, the color bar represents the two-way travel time of the structural map time.

279x215mm (300 x 300 DPI)

DOI: 10.1190/INT-2021-0061.1

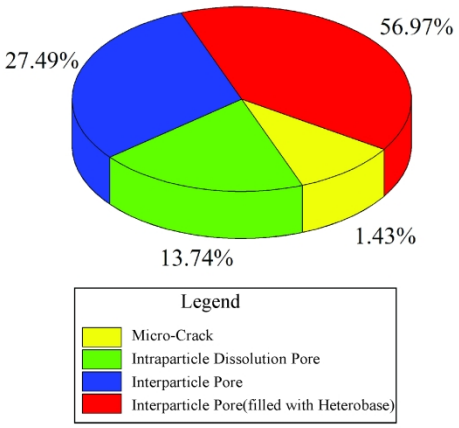

Figure 4

Figure 4. The statistics of reservoir porosity type based the cores of the X2 formation. The main pore type is inter-particle pores filled with heterobase.

279x215mm (300 x 300 DPI)

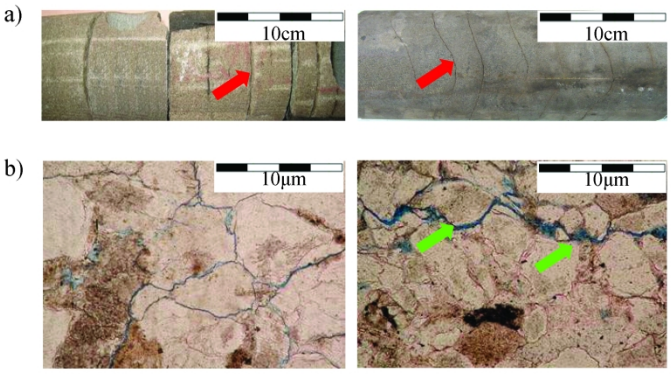

Figure 5

Figure 5. (a) Representative cores and (b) thin sections of the X2 formation. (a) The cores with horizontal and low dipping angle fractures (indicated by the red arrows). (b) The thin section demonstrating the dissolved pores that were filled by the blue feldspars (indicated by the green arrows) and micro fractures.

279x215mm (300 x 300 DPI)

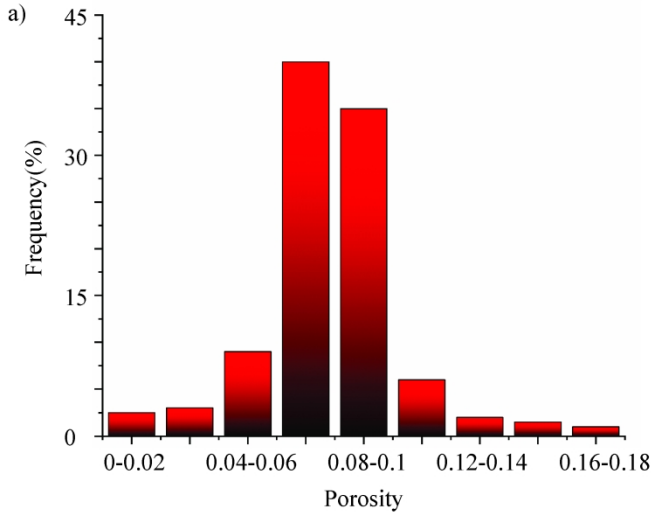

Figure 6a

Figure 6a. Histogram of (a) the core porosity and (b) core permeability of the X2 formation.

279x215mm (300 x 300 DPI)

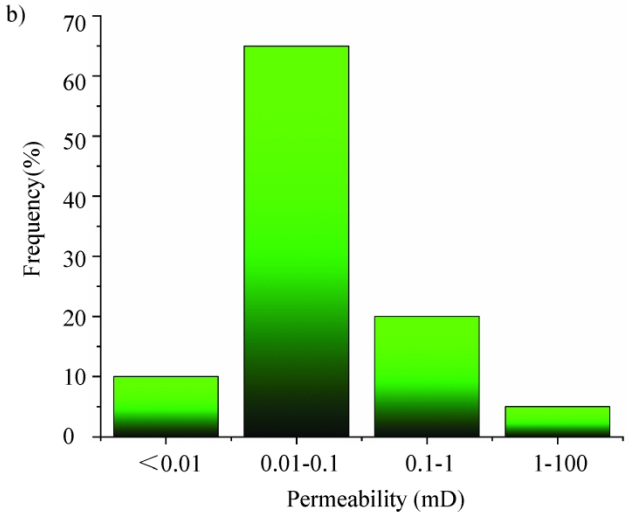

Figure 6b

Figure 6b. Histogram of (a) the core porosity and (b) core permeability of the X2 formation.

279x215mm (300 x 300 DPI)

DOI: 10.1190/INT-2021-0061.1

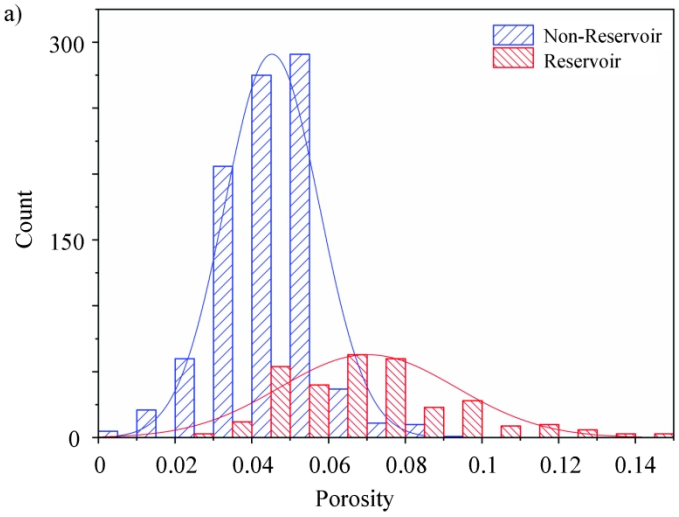

Figure 7a

Figure 7a. The histogram of porosity and P-wave logs for the X2 formation. (a)Histogram of porosity log. (b)Histogram of logging P-wave. The blue and red bars are the histogram for the well logs of non-reservoir and reservoir, respectively.

279x215mm (300 x 300 DPI)

DOI: 10.1190/INT-2021-0061.1

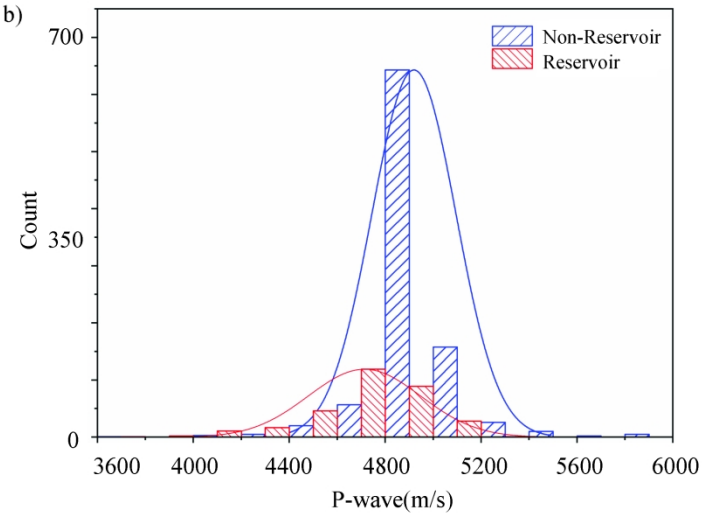

Figure 7b

Figure 7b. The histogram of porosity and P-wave logs for the X2 formation. (a)Histogram of porosity log. (b)Histogram of logging P-wave. The blue and red bars are the histogram for the well logs of non-reservoir and reservoir, respectively.

279x215mm (300 x 300 DPI)

DOI: 10.1190/INT-2021-0061.1

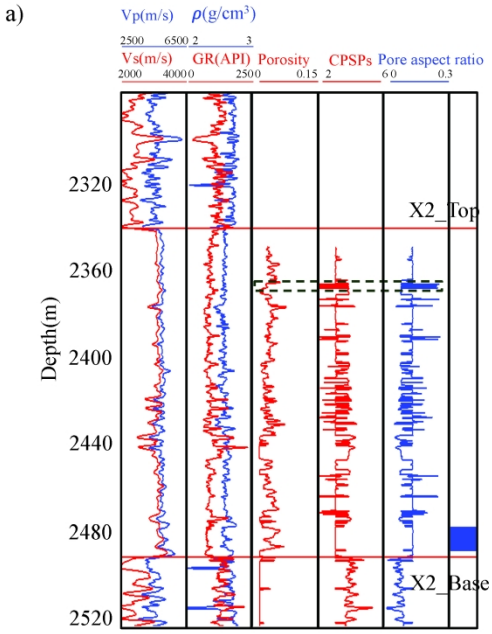

Figure 8a

Figure 8a. The well logs of (a) YJ3, (b) YJ2, and (c) YJ2. The red and blue curves in the first panel are P-wave and S-wave velocities, respectively. The red and blue curves in the second panel are density and Gamma-Ray logs. The third, fourth, and fifth panel are porosity, CPS, and pore aspect ratio, respectively. The red and blue blocks in the sixth panel represent high and low production zones.

279x215mm (300 x 300 DPI)

DOI: 10.1190/INT-2021-0061.1

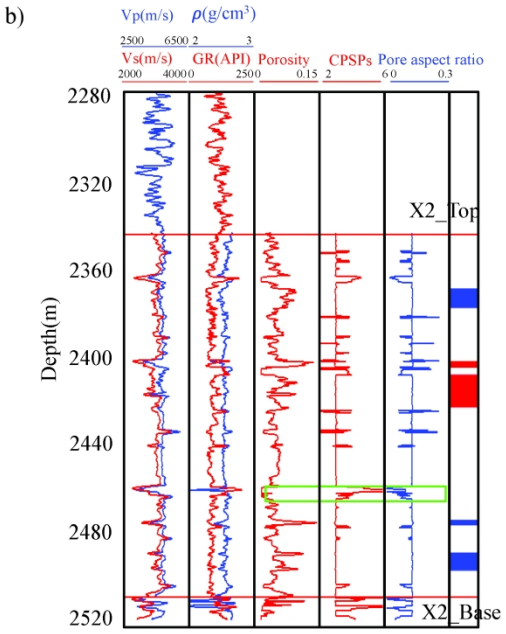

Figure 8b

Figure 8b. The well logs of (a) YJ3, (b) YJ2, and (c) YJ2. The red and blue curves in the first panel are P-wave and S-wave velocities, respectively. The red and blue curves in the second panel are density and Gamma-Ray logs. The third, fourth, and fifth panel are porosity, CPS, and pore aspect ratio, respectively. The red and blue blocks in the sixth panel represent high and low production zones.

279x215mm (300 x 300 DPI)

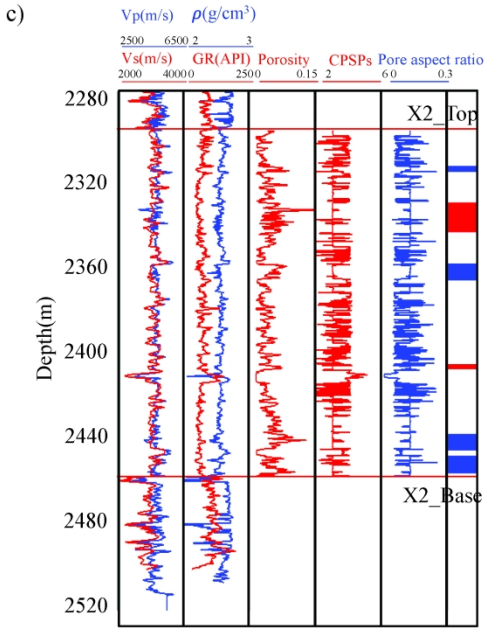

Figure 8c

Figure 8c. The well logs of (a) YJ3, (b) YJ2, and (c) YJ2. The red and blue curves in the first panel are P-wave and S-wave velocities, respectively. The red and blue curves in the second panel are density and Gamma-Ray logs. The third, fourth, and fifth panel are porosity, CPS, and pore aspect ratio, respectively. The red and blue blocks in the sixth panel represent high and low production zones.

279x215mm (300 x 300 DPI)

DOI: 10.1190/INT-2021-0061.1

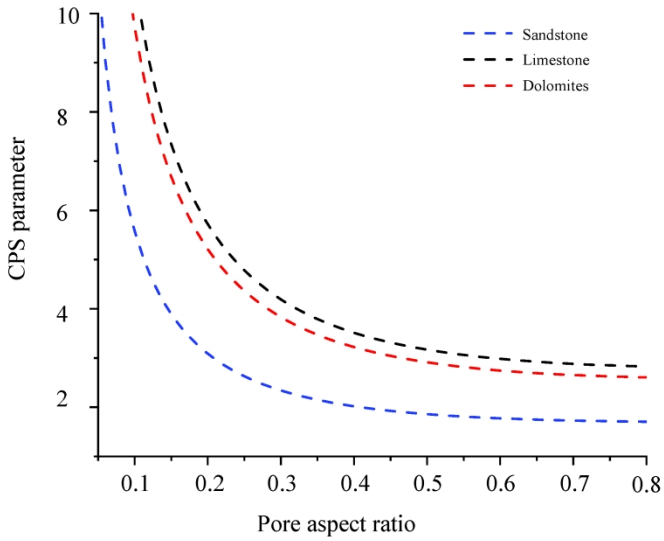

Figure 9

Figure 9. The CPS parameter varying with pore aspect ratio for different lithologies. The red, blue, and black dash lines show the CPS parameter varies with pore aspect ratio for dolomites, sandstone, and limestone, respectively

279x215mm (300 x 300 DPI)

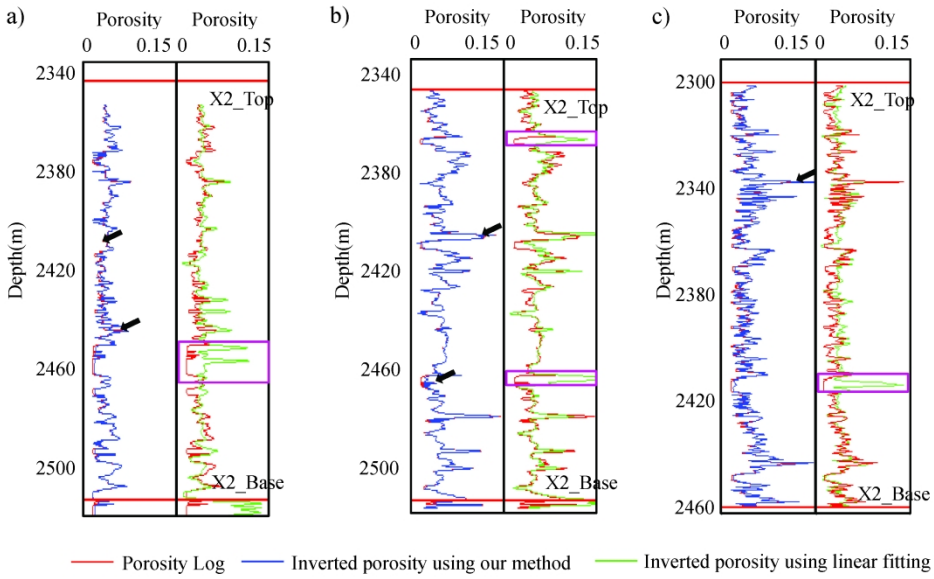

Figure 10

Figure 10. The comparison of predicted porosity at well (a) YJ3, (b) well YJ1, and (c) YJ2, respectively. The red, blue, and green curves are the porosity log, predicted porosity using our method, and inverted porosity using learning fitting. The black arrows indicate the negligible errors produced by our method. The purple rectangles indicate the obvious inaccurate prediction using linear fitting.

279x215mm (300 x 300 DPI)

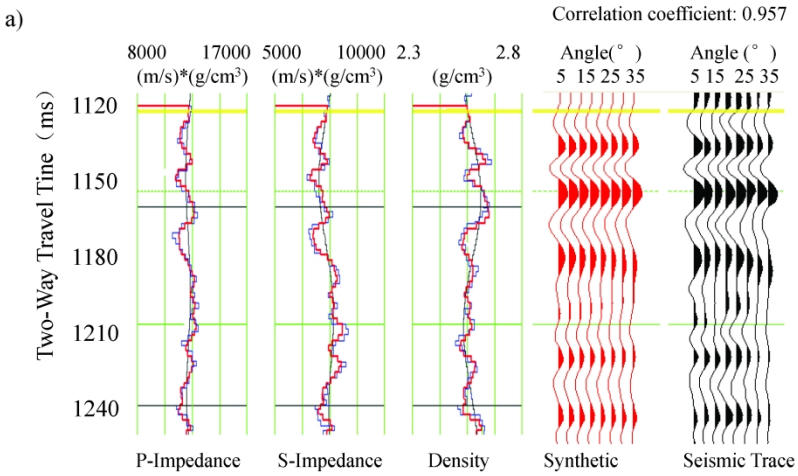

Figure 11a

Figure 11a. Prestack AVO inversion analysis at (a)YJ1 and (b)YJ3 well. The red, blue, and black curves are the inverted, original well log, and low-frequency component of well log, respectively. The red and black seismic traces are the synthetic and real seismic data.

279x215mm (300 x 300 DPI)

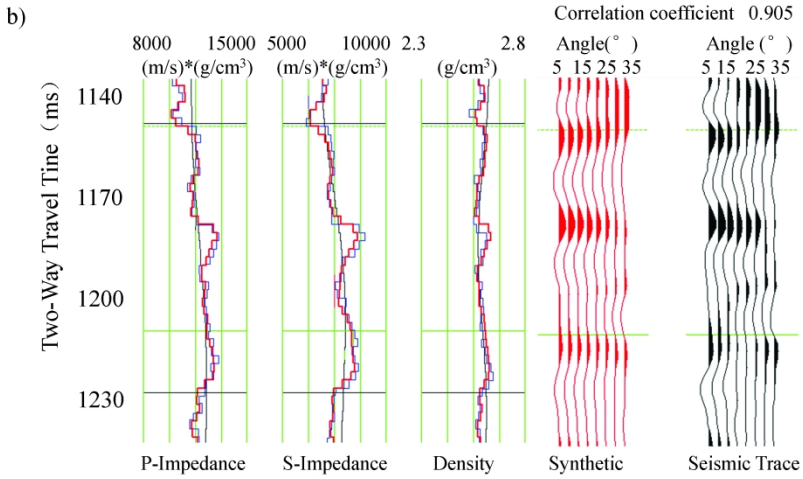

Figure 11b

Figure 11b. Prestack AVO inversion analysis at (a)YJ1 and (b)YJ3 well. The red, blue, and black curves are the inverted, original well log, and low-frequency component of well log, respectively. The red and black seismic traces are the synthetic and real seismic data.

279x215mm (300 x 300 DPI)

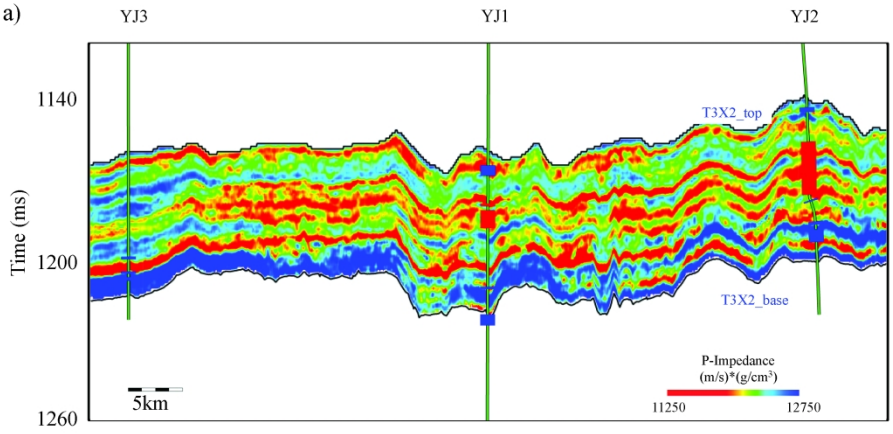

Figure 12a

Figure 12a. The inverted sections of (a) P-impedance, (b)S-impedance and (c)Density. The gas (red square) and low gas producing layers (blue square) correspond to the low impedance and density area.

279x215mm (300 x 300 DPI)

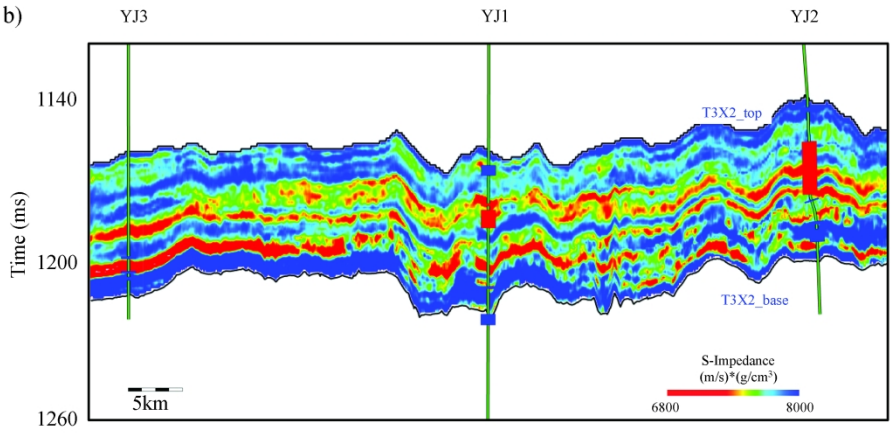

Figure 12b

Figure 12b. The inverted sections of (a) P-impedance, (b)S-impedance and (c)Density. The gas (red square) and low gas producing layers (blue square) correspond to the low impedance and density area.

279x215mm (300 x 300 DPI)

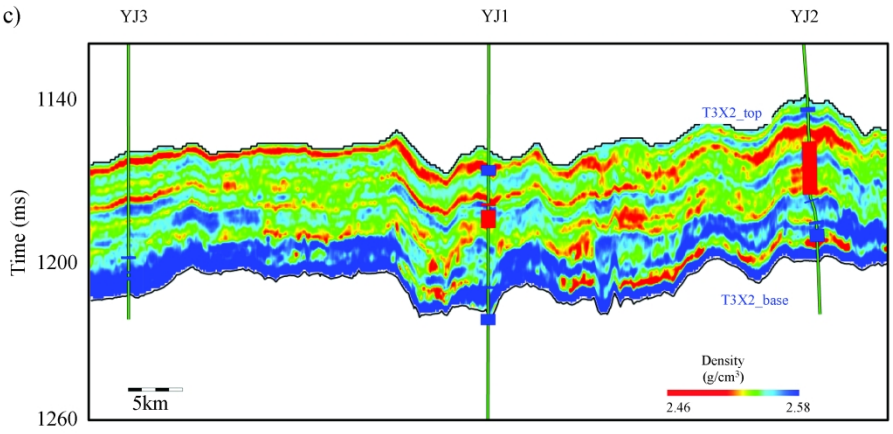

Figure 12c

Figure 12c. The inverted sections of (a) P-impedance, (b)S-impedance and (c)Density. The gas (red square) and low gas producing layers (blue square) correspond to the low impedance and density area.

279x215mm (300 x 300 DPI)

DOI: 10.1190/INT-2021-0061.1

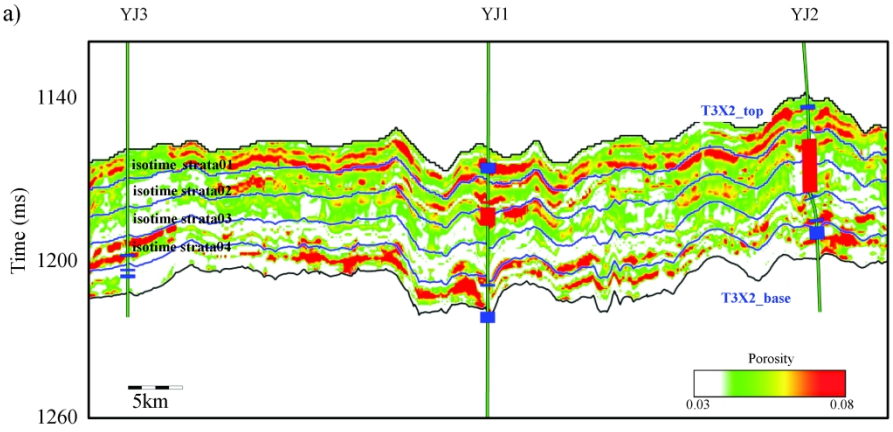

Figure 13a

Figure 13a. The vertical section of predicted porosity using (a) proposed method, (b) probabilistic neural network, (c) multi-layer feed forward network, and (d) the Eshelby-Walsh model, respectively. The horizontal blue curves are the strata horizons. The red and blue arrows indicate high and low production zones.

279x215mm (300 x 300 DPI)

DOI: 10.1190/INT-2021-0061.1

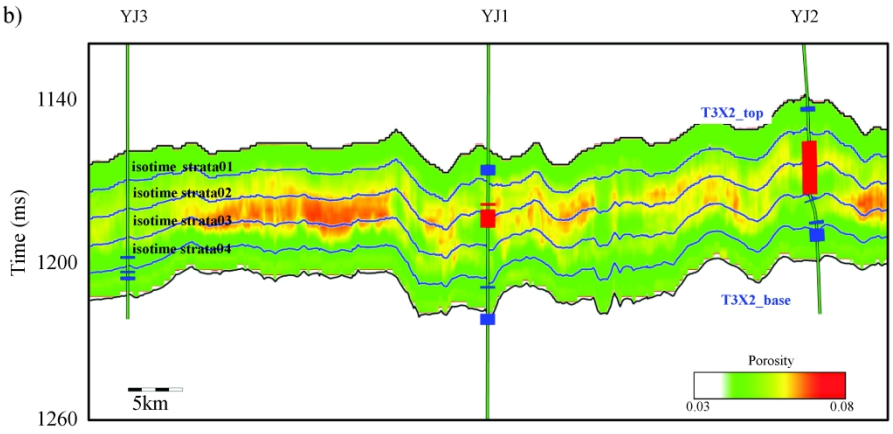

Figure 13b

Figure 13b. The vertical section of predicted porosity using (a) proposed method, (b) probabilistic neural network, (c) multi-layer feed forward network, and (d) the Eshelby-Walsh model, respectively. The horizontal blue curves are the strata horizons. The red and blue arrows indicate high and low production zones.

279x215mm (300 x 300 DPI)

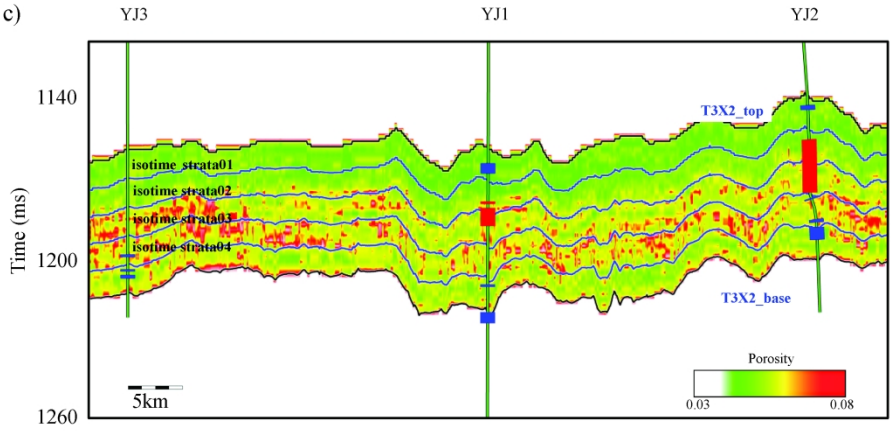

Figure 13c

Figure 13c. The vertical section of predicted porosity using (a) proposed method, (b) probabilistic neural network, (c) multi-layer feed forward network, and (d) the Eshelby-Walsh model, respectively. The horizontal blue curves are the strata horizons. The red and blue arrows indicate high and low production zones.

279x215mm (300 x 300 DPI)

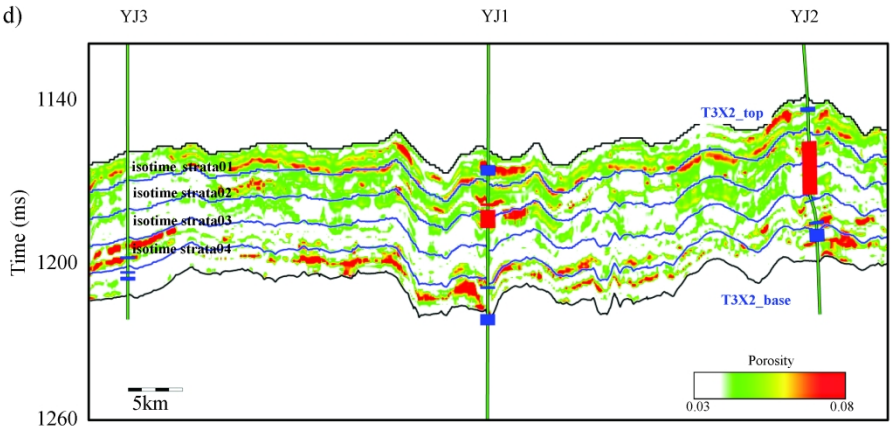

Figure 13d

Figure 13d. The vertical section of predicted porosity using (a) proposed method, (b) probabilistic neural network, (c) multi-layer feed forward network, and (d) the Eshelby-Walsh model, respectively. The horizontal blue curves are the strata horizons. The red and blue arrows indicate high and low production zones.

279x215mm (300 x 300 DPI)

DOI: 10.1190/INT-2021-0061.1

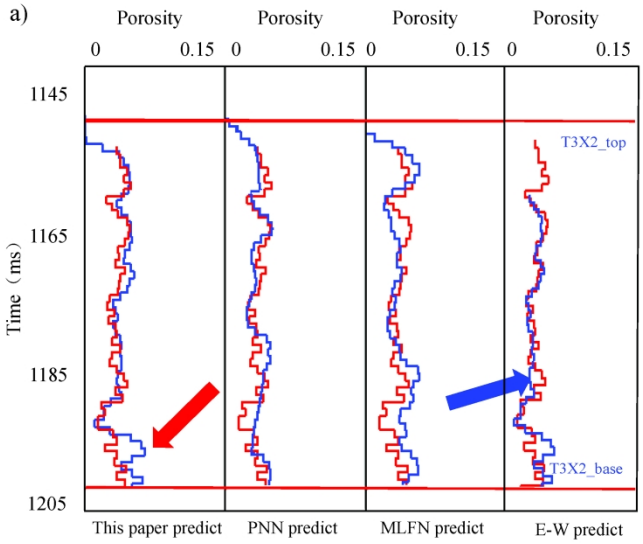

Figure 14a

Figure 14a. The comparison of predicted porosities (red curves) and porosity log (blue curves) at (a) well YJ3, (b) well YJ1, and (c) YJ2. The blue curves in the first, second, third, fourth panels are predicted porosity using proposed method, PNN, MLFN, and E-W model, respectively. The red, blue and green arrows indicate the zones that has relatively high predicted error.

279x215mm (300 x 300 DPI)

DOI: 10.1190/INT-2021-0061.1

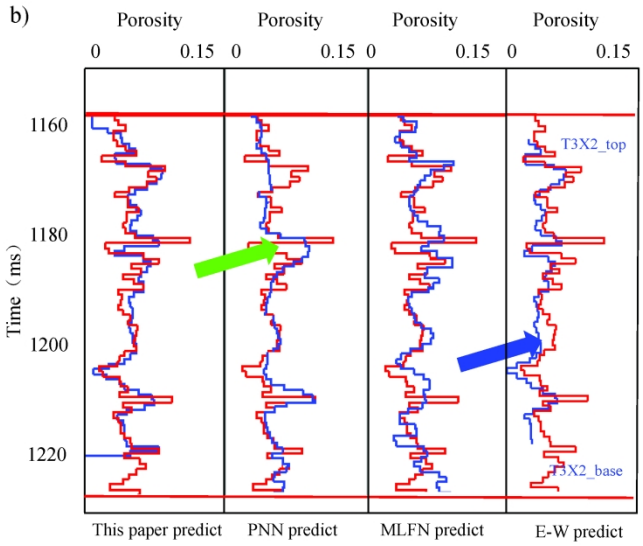

Figure 14b

Figure 14b. The comparison of predicted porosities (red curves) and porosity log (blue curves) at (a) well YJ3, (b) well YJ1, and (c) YJ2. The blue curves in the first, second, third, fourth panels are predicted porosity using proposed method, PNN, MLFN, and E-W model, respectively. The red, blue and green arrows indicate the zones that has relatively high predicted error.

279x215mm (300 x 300 DPI)

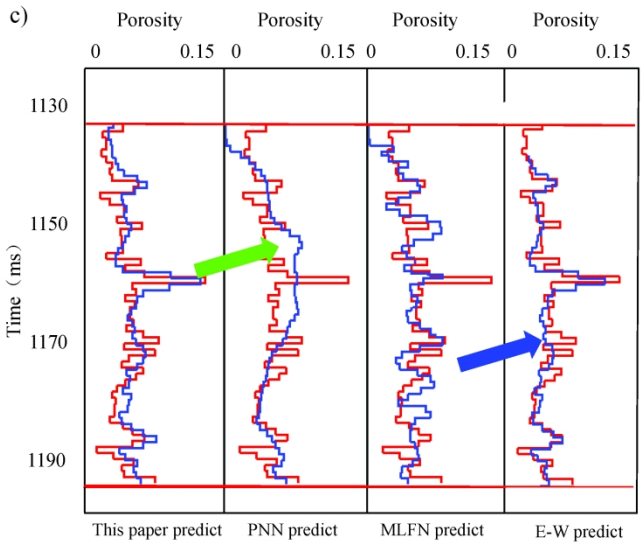

Figure 14c

Figure 14c. The comparison of predicted porosities (red curves) and porosity log (blue curves) at (a) well YJ3, (b) well YJ1, and (c) YJ2. The blue curves in the first, second, third, fourth panels are predicted porosity using proposed method, PNN, MLFN, and E-W model, respectively. The red, blue and green arrows indicate the zones that has relatively high predicted error.

279x215mm (300 x 300 DPI)

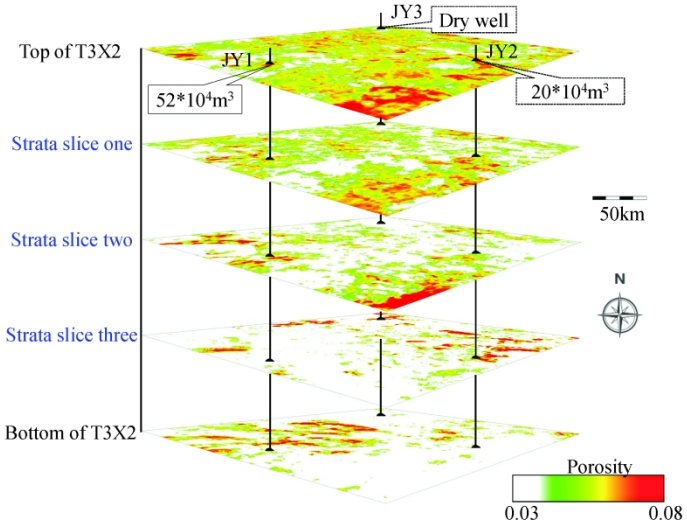

Figure 15

Figure 15. The strata slices of predicted porosity within the target zones.

279x215mm (300 x 300 DPI)

DOI: 10.1190/int-2021-0061.1

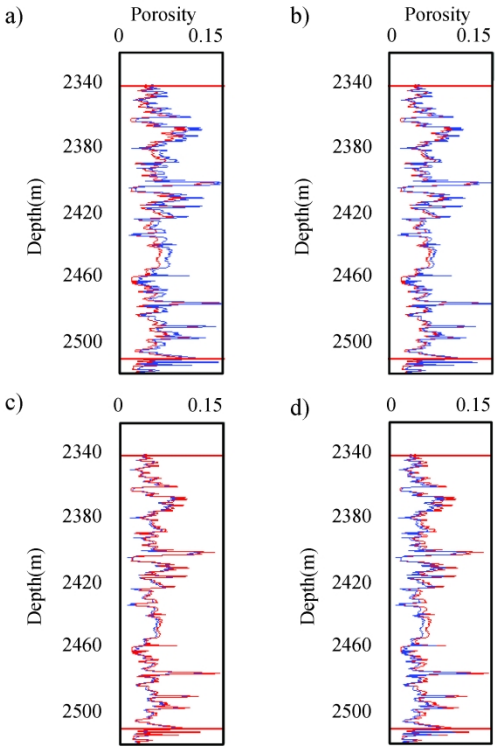

Figure 16

Figure 16. The sensitive analysis for the effect of CPS parameter on porosity prediction. We perturbation the CPS with (a)-20 %, (b) -10 %, (c) 10 %, and (d) 20 %. The red curves are the porosity log and blue curves are predicted porosity using our method, respectively.

279x215mm (300 x 300 DPI)

DOI: 10.1190/int-2021-0061.1

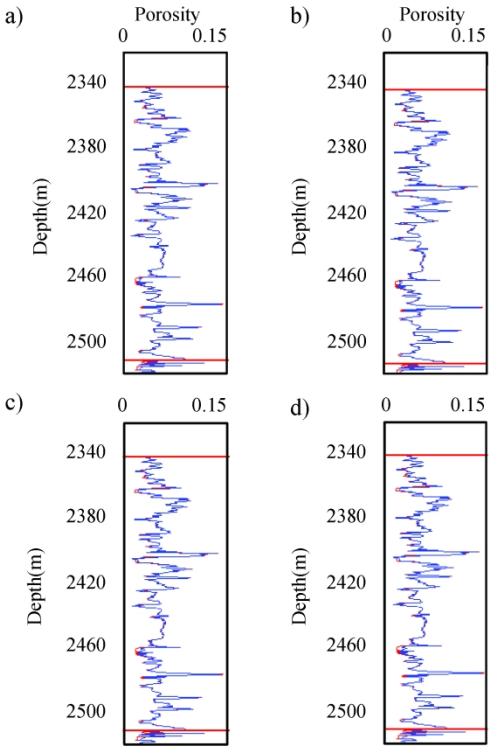

Figure 17

Figure 17. The sensitive analysis for the effect of fluid modulus on porosity prediction. We perturbation the fluid modulus with (a)-20 %, (b) -10 %, (c) 10 %, and (d) 20 %. The red curves are the porosity log and blue curves are predicted porosity using our method, respectively.

279x215mm (300 x 300 DPI)

DOI: 10.1190/INT-2021-0061.1

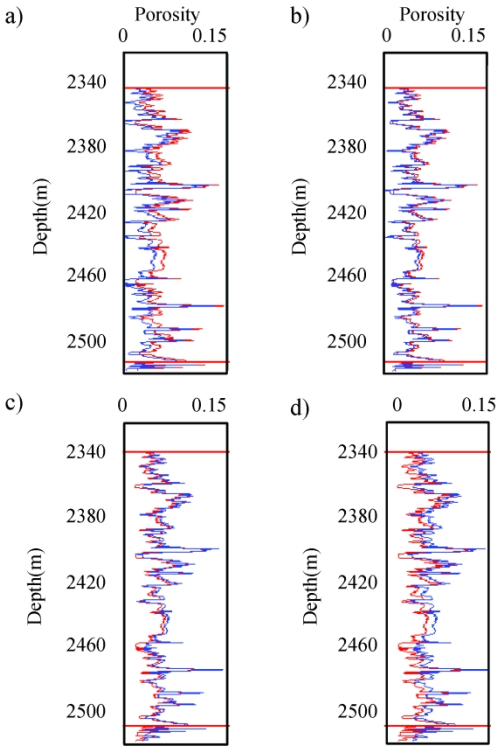

Figure 18

Figure 18. The sensitive analysis for the effect of matrix modulus on porosity prediction. We perturbation the matrix modulus with (a)-20 %, (b) -10 %, (c) 10 %, and (d) 20 %. The red curves are the porosity log and blue curves are predicted porosity using our method, respectively.

279x215mm (300 x 300 DPI)

Table 1. The Relationship between the skeleton general formula and different dry frame modulus models.

He's model	p	q	$q/(p+q)$
Eshelby-Walsh	0	m/α	1
Pride	1	c	~1
Nur	$1/\phi_c$	0	0
Hou	$1/\phi_c$	c/ϕ_c	~1

Table 2. Parameters of the pure quartz model, gas-bearing reservoir, $K_{fl}$is the bulk modulus of gas.

Model parameter	**Value**
K_0(GPa)	37
μ_0 (GPa)	44
ρ_0 (g/cm^3)	2.65
K_{fl} (GPa)	0.336
ρ_{fl} (g/cm^3)	0.04
ϕ	0.01–0.1
α	0.2–0.8

DATA AND MATERIALS AVAILABILITY

Data associated with this research are confidential and cannot be released.

DOI:10.1190/int-2021-0001.1